Article:

Mangan, TP orcid.org/0000-0001-7053-5594, Douglas, KM orcid.org/0000-0002-3281-3685, Lade, RE orcid.org/0000-0003-1773-5655 et al. (3 more authors) (2021) Kinetic Study of the Reactions of AlO with H2O and H2; Precursors to Stellar Dust Formation. ACS Earth and Space Chemistry, 5 (12). pp. 3385-3395. ISSN 2472-3452

https://doi.org/10.1021/acsearthspacechem.1c00225

Kinetic study of the reactions of AlO with H_2O and H_2; precursors to stellar dust formation

Thomas P. Mangan[1], Kevin M. Douglas[1], Rachel E. Lade[1], David Gobrecht[2], Leen Decin[1, 2] and John M. C. Plane*[1]

[1] School of Chemistry, University of Leeds, Woodhouse Lane, Leeds LS2 9JT, UK.

[2] Department of Physics and Astronomy, Institute of Astronomy, KU Leuven, Celestijnenlaan 200 D, B-3001 Leuven (Heverlee), Belgium.

*corresponding author. Email: j.m.c.plane@leeds.ac.uk

Keywords: aluminium oxide reactions; laser-based kinetic technique; RRKM theory; Master equation analysis; electronic structure theory; AGB stars; stellar outflow chemistry; alumina dust formation

Abstract

AlO is relatively abundant around oxygen-rich Asymptotic Giant Branch (AGB) stars, where it can react with abundant gas-phase species such as H_2 and H_2O to form AlOH. These Al-containing species are the likely precursors of refractory alumina nano-particles, which may provide the nuclei for dust formation. In the present study, the kinetics of these AlO reactions were measured from 295 - 780 K using the pulsed laser photolysis of $Al(C_5H_7O_2)_3$, with time-resolved laser induced fluorescence detection of AlO. The experimental results were interpreted using quantum chemistry calculations and a Master Equation solver for reactions with multiple energy wells. For the recombination reaction $AlO + H_2O (+ N_2) \rightarrow Al(OH)_2$, $\log_{10}(k_{rec,0} / \text{cm}^6 \text{ molecule}^{-2} \text{ s}^{-1}) = -32.9185 + 8.80276 \log_{10}(T) - 2.4723(\log_{10}(T))^2$; $\log_{10}(k_{rec,\infty} / \text{cm}^3 \text{ molecule}^{-1} \text{ s}^{-1}) = -19.4686 + 7.62037 \log_{10}(T) - 1.47214(\log_{10}(T))^2$; $Fc = 0.28$ (uncertainty ±13% from 295 – 760 K). For the bimolecular reactions, $k(AlO + H_2O \rightarrow AlOH + OH) = (3.89\pm0.47) \times 10^{-10} \exp(-(1295\pm150)/T)$ and $k(AlO + H_2 \rightarrow AlOH + H) = (5.37\pm0.52) \times 10^{-13} (T/300)^{(2.77\pm0.19)} \exp(-(2190\pm110)/T)$ cm^3 molecule^{-1} s^{-1}. Rate coefficients for $Al + H_2O \rightarrow AlOH + H$, $AlOH + H \rightarrow AlO + H_2$ or $Al + H_2O$, and the absorption cross sections of AlOH and AlO, were calculated theoretically. Al chemistry around an O-rich AGB star was then investigated using a β-trajectory model, which predicts that AlOH is the major gas-phase Al species beyond two stellar radii, and shows that the relative AlO abundance is very sensitive to the AlOH photolysis rate.

Introduction

Asymptotic Giant Branch (AGB) stars are evolved stars experiencing significant mass loss at the end of their lifecycle. Within the CircumStellar Envelope (CSE) around an AGB star, gas-phase chemistry produces thermally stable molecules which aggregate and condense into dust particles as the gas cools, forming an optically thick shell.[1] The release of molecules and dust formation in the CSEs around AGB stars are a major source of dust grains in the universe.[2]

A range of candidates has been proposed for the primary initial dust grains around oxygen-rich AGB stars (i.e. $C/O < 1$), including metal titanates, metal silicates, SiO and Al_2O_3 (alumina).[3, 4] Many infra-red (IR) spectra of O-rich CSEs suggest that O-rich dust such as silicates, and especially alumina, are likely candidates for the initial dust grains.[4] Alumina is particularly favoured as an initial dust seed in the inner wind of O-rich AGB stars due to its refractory nature and high condensation temperature (around 1400 K).[5] A broad emission band at 11 μm in the IR spectra of many O-rich AGB stars is widely thought to come from amorphous Al_2O_3.[6, 7] Begemann *et al.* [8] determined the optical constants of alumina particles and showed that a feature at 13 μm might arise from crystalline α-Al_2O_3 (corundum), although Posch *et al.* [9] suggested $MgAl_2O_4$ (spinel) as a more likely carrier. Subsequently, Sloan *et al.* [10] used correlations between IR spectra to argue that the 13 μm band arises from crystalline Al_2O_3. When modelling the CSEs of a group of 37 AGB stars in the Large Magellanic Cloud, Jones *et al.* [11] found that an appreciable fractional abundance of alumina in dust (up to 50%) improved the fitting of IR spectra. For AGB stars S Ori and R Cnc, Karovicova *et al.* [5] were able to describe the observed spectra with a pure alumina dust shell.

A range of Al-containing species has been observed around AGB stars, with AlO and AlOH the most abundant.[7, 12, 13, 14] AlO has also been detected in the CSE of the young, massive star Orion Source I.[15] These relatively abundant Al species are thought to be the direct precursors to alumina dust, with Gobrecht *et al.* [16] proposing that AlO undergoes dimerization to $(AlO)_2$, which is then oxidized to Al_2O_3. The Al_2O_3 then itself dimerizes before clustering further and condensing to form dust grains. Other reaction pathways to alumina may be possible, including reactions involving AlO, AlOH and $Al(OH)_2$ with other gas-phase species.[17]

Decin *et al.* [14] found that the variable chemistry of AGB stars leads to differences in the fractional abundances of AlO and AlOH, with both species apparent at distances from the star both before and after dust condensation occurs. For example, AlOH is more readily detected than AlO in the CSE of high mass-loss Mira-type O-rich star IK Tau, while conversely AlO is approximately 70 times more abundant in the CSE of the low mass-loss rate semi-regular O-rich AGB star R Dor. In the O-rich red supergiant VY CMa, AlOH was found to be 17 times more abundant than AlO.[12] Understanding the gas-phase chemistry between AlO and AlOH in CSEs (where temperatures in the dust formation region are around 500 – 2000 K) is crucial to understanding the variable chemistry observed from star to star and in understanding the initial steps of how dust forms around AGB stars.

H_2O is one of the more abundant reactive species around O-rich AGB stars; e.g. the relative abundance of H_2O to H_2 at IK Tau is 6.6×10^{-5}.[18] H_2O could react with AlO in a termolecular recombination reaction:

$$AlO + H_2O\ (+\ M) \rightarrow Al(OH)_2 \qquad \Delta H^\circ(0\ K) = -307\ kJ\ mol^{-1} \qquad (R1a)$$

where M is the bath gas (H_2 in the case of stellar chemistry). Reactions of this type should become slower with increasing temperature, and should be pressure-dependent. Therefore, in the relatively low pressure and high temperature environment close to an AGB star it may be a minor removal pathway for AlO, while bimolecular reaction channels may become more important:

$$\mathrm{AlO + H_2O \rightarrow AlOH + OH} \qquad \Delta H^\circ(0\ \mathrm{K}) = 15\ \mathrm{kJ\ mol^{-1}} \tag{R1b}$$

$$\mathrm{\rightarrow OAlOH + H} \qquad \Delta H^\circ(0\ \mathrm{K}) = 26\ \mathrm{kJ\ mol^{-1}} \tag{R1c}$$

$$\mathrm{\rightarrow OAlO + H_2} \qquad \Delta H^\circ(0\ \mathrm{K}) = 111\ \mathrm{kJ\ mol^{-1}} \tag{R1d}$$

Depending on the specific AGB star, H_2 is 4 - 10 orders of magnitude more abundant than any other species, and so could provide another possible pathway to AlOH formation via R2a:

$$\mathrm{AlO + H_2 \rightarrow AlOH + H} \qquad \Delta H^\circ(0\ \mathrm{K}) = -41\ \mathrm{kJ\ mol^{-1}} \tag{R2a}$$

$$\mathrm{\rightarrow Al + H_2O} \qquad \Delta H^\circ(0\ \mathrm{K}) = 20\ \mathrm{kJ\ mol^{-1}} \tag{R2b}$$

The reactions

$$\mathrm{Al + H_2O \rightarrow AlOH + H} \qquad \Delta H^\circ(0\ \mathrm{K}) = -61\ \mathrm{kJ\ mol^{-1}} \tag{R3a}$$

$$\mathrm{\rightarrow AlO + H_2} \qquad \Delta H^\circ(0\ \mathrm{K}) = 20\ \mathrm{kJ\ mol^{-1}} \tag{R3b}$$

and

$$\mathrm{AlOH + H \rightarrow AlO + H_2} \qquad \Delta H^\circ(0\ \mathrm{K}) = 41\ \mathrm{kJ\ mol^{-1}} \tag{4a}$$

$$\mathrm{\rightarrow Al + H_2O} \qquad \Delta H^\circ(0\ \mathrm{K}) = 61\ \mathrm{kJ\ mol^{-1}} \tag{4b}$$

take place on the same potential energy surface (PES) as R2, and are likely to be important in outflow chemistry because of the relatively large abundances of H_2O and H. The enthalpy changes (at 0 K) listed above for these reactions are calculated at the G4 level of theory [19, 20] (see the Discussion). All of these bimolecular reaction channels (apart from R1d which is significantly endothermic compared to the other channels of R1) could potentially influence the gas-phase abundances of AlO and AlOH around AGB stars, and hence the rate of alumina dust formation in their CSEs.

Another reason for studying reaction 1 concerns the chemistry of Al which ablates from cosmic dust entering planetary atmospheres.[21, 22] Al atoms react rapidly with O_2 to form AlO,[23] which can then recombine with H_2O at the comparatively lower temperatures (< 300 K) and higher pressures (~ 10^{-6} bar) typical of the atmospheric region in which ablation occurs.[24] In our recent study of the chemistry of meteor-ablated Al in the Earth's upper mesosphere, we used quantum calculations to show that AlOH may have a large photolysis cross section below 260 nm, and this would significantly change the AlO/AlOH ratio.[22] AlOH photolysis is also likely to be important in the inner region of a stellar outflow, before the stellar radiation is obscured by dust formation.

To the best of our knowledge, the reaction kinetics of AlO with H_2O has not been studied previously, and only an upper limit for AlO + H_2 of 5×10^{-14} cm^3 molecule^{-1} s^{-1} has been reported at 298 K.[25] The reaction of Al with H_2O has been studied from 298-1174 K,[26] though the products were not identified. There do not appear to be any experimental studies of the reaction between AlOH and H.

In the present study we report kinetic measurements of R1 and R2 at temperatures up to 780 K. A combination of electronic structure calculations and Rice-Ramsperger-Kassel-Markus (RRKM) theory is then used to extrapolate the experimental results over the full temperature range (150 – 2000 K) pertinent to both planetary atmospheres and dust formation around AGB stars (500 - 2000 K), as well as predicting the reaction products. Reactions R3 and R4 are explored in the same way. In the final part of the Discussion we explore the impact of these reactions, together with AlOH photolysis, on the ratio of AlO to AlOH around two examples of AGB stars.

Experimental

Reactions R1 and R2 were studied using the pulsed laser photolysis-laser induced fluorescence (PLP-LIF) technique within a temperature-controlled reactor (192 – 1100 K). A schematic diagram of the experimental layout is shown in Figure 2 of Mangan *et al.* [27] AlO molecules were produced in the reactor by the multiphoton dissociation of aluminium acetylacetonate ($Al(C_5H_7O_2)_3$, also known as $Al(acac)_3$) vapor by a loosely focused KrF excimer laser (Physik COMPEX 102) at 248 nm, with a typical pulse energy of 40 mJ at 10 Hz (< 5 mJ in the reactor). Solid $Al(acac)_3$ powder was inserted into one of the chamber arms, contained in a steel boat attached to the end of a thermocouple (K-type), and heated to ~340-370 K using heating tape around the reactor arm in order to achieve a sufficient $Al(acac)_3$ vapour pressure, estimated to be 2.4×10^{-4} Torr at 340 K.[28] A flow of N_2 over the steel boat entrained and transported the $Al(acac)_3$ vapour into the main reactor volume. Experiments were conducted up to a maximum temperature around 780 K; above this temperature the LIF signal degraded, presumably due to decomposition of the $Al(acac)_3$ precursor in the reactor.

The transition probed by LIF was the AlO ($B^2\Sigma^+$ - $X^2\Sigma^+(0,0)$) band at 484.23 nm [29] using a Nd:YAG (Quantel Q smart 850 at 355 nm) pumped dye laser (Sirah Cobra-stretch CBST-G-18) with Coumarin 102 laser dye. The time delay between the counter-propagating dye laser (probe) and excimer laser (photolysis, $t = 0$) beams was varied to produce scans of the relative AlO concentration with time. Typical kinetic traces were produced from 1000 laser shots, with an accumulation time of 100 s. The AlO LIF signal was collected using a photomultiplier tube (Electron Tubes, model 9816QB) positioned orthogonal to the laser beams, through an interference filter (λ_{max} = 480 nm, fwhm = 10 nm).

A total gas flow through the reactor of 180 - 600 sccm included the $Al(acac)_3$ vapor entrained in the bath gas, the reactant gas (H_2O or H_2) and a balancing flow of the bath gas (either N_2 or He). These flows were set using calibrated mass flow controllers, and the pressure in the reactor (4 – 24 Torr) measured with a capacitance manometer. The AlO concentration in the reactor was estimated to be $\leq 10^{11}$ molecule cm^{-3}, based on the vapour pressure of $Al(acac)_3$ in the reactor side-arm (see above) being diluted by the other flows entering the reactor, and assuming at most 1% photolysis producing AlO. This AlO concentration was several orders of magnitude lower than the concentrations of H_2O or H_2 in the reactor (e.g. $[H_2O] = (0.02 - 1) \times 10^{15}$ molecule cm^{-3}) to ensure pseudo first-order conditions, consistent with the observed single exponential decays of AlO (see Results).

In the case of experiments studying R1, after each change of the H_2O gas flow the reactor was conditioned for 30 minutes. Repeat measurements of the first-order rate of AlO removal, taken several minutes apart, were used to confirm that the concentration of H_2O vapor in the reactor had reached a steady state, at which point the concentration was assumed to be consistent with that of the H_2O/N_2 mixture made up on the glass gas-handling line.

Materials. N_2 (99.9999% pure, Air Products) and He (99.9999 % pure, BOC) were used without any further purification. H_2 (99.99 % pure, BOC) was flowed through a liquid N_2 cold trap. H_2O vapor was produced by freeze-pump thawing deionized water for three cycles and subsequent dilution with N_2 in a glass bulb. $Al(acac)_3$ (99% pure, Sigma Aldrich) was warmed under vacuum in the reactor for at least 30 mins prior to experiments.

Results

AlO + H_2O

The time-resolved LIF signals of AlO are described by a single exponential form $A.\exp(-k't)$, where t is the time delay between the photolysis and probe lasers and k' is the pseudo first-order decay coefficient. In the case of reaction R1, the rate equation is given by:

$$k' = k_{\text{diff}} + k_{1a}[\text{H}_2\text{O}][\text{N}_2] + (k_{1b} + k_{1c} + k_d)[\text{H}_2\text{O}] \qquad \text{(E1)}$$

where k_{diff} is the rate of diffusion of AlO molecules out of the photolysis volume observed by the PMT, as well as any reaction between AlO and the Al(acac)$_3$ precursor. As R1a is a termolecular reaction the rate should be dependent on both the reactant [H_2O] and bath gas [N_2]. Shown in the example kinetic trace of Figure 1 (and consistent with previous reactions studied in Mangan *et al.* [30]), AlO is rapidly and directly made by photolysis of the precursor in the absence of an O_2 flow, with the LIF signal peaking within ~ 40 μs. The more gradual rise in the AlO LIF signal near the peak is likely caused by quenching of rovibrationally excited AlO.[25] The kinetic traces were fitted at longer times ($\geq$ 100 μs) after which relaxation of the excited states no longer significantly affects the single exponential nature of the decay, ensuring pseudo first-order behaviour was observed.

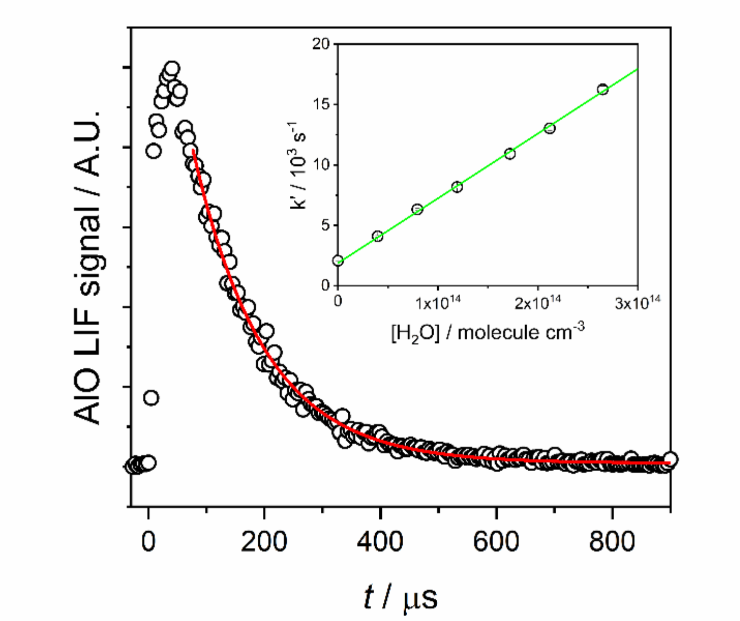

Figure 1. Kinetic trace showing AlO LIF signal after PLP at $t = 0$ μs of Al(acac)$_3$ for [H_2O] = 1.19×10^{14} molecules cm^{-3} at 590 K with a total pressure of 8.9 Torr. The inset shows the associated bimolecular plot for R1 at all [H_2O] measured at these conditions with k_1 = $(5.36 \pm 0.55) \times 10^{-11}$ cm^3 molecule^{-1} s^{-1}.

Shown in the inset of Figure 1 is a plot of k' against [H_2O], taken at 8.9 Torr at 590 K. The slope of the linear fit provides the second order-rate coefficient k_1. The full set of measured values are provided in Table S1 of the Supplementary Information. As was seen in Mangan *et al.* [30], the non-zero intercept k_{diff} is higher than the expected diffusion rate for AlO in N_2 under these conditions,[27] because AlO is likely reacting with the precursor (or possibly a fragment of Al(acac)$_3$ at higher temperatures). Repeat measurements of k' in the absence of reactant at the beginning and end of each set of experiments were consistent within error. The second-order rate coefficients were also independent of both gas residence time in the reactor (0.1 - 1 s) and the precursor concentration, suggesting no interaction between the precursor and H_2O.

Figure 2 shows the pressure dependence of k_1 over the temperature range 295–760 K. At 295 K the reaction exhibits clear fall-off behaviour over the pressure range studied (3.2 - 12.1 Torr), indicating that R1a is the dominant channel, and this also explains the negative T-dependence up to 590 K. At higher temperatures the reaction exhibits little pressure dependence and switches to a positive T-dependence, indicating that one or more of the bimolecular reaction channels 1b – 1d has opened. This is explored further in the Discussion.

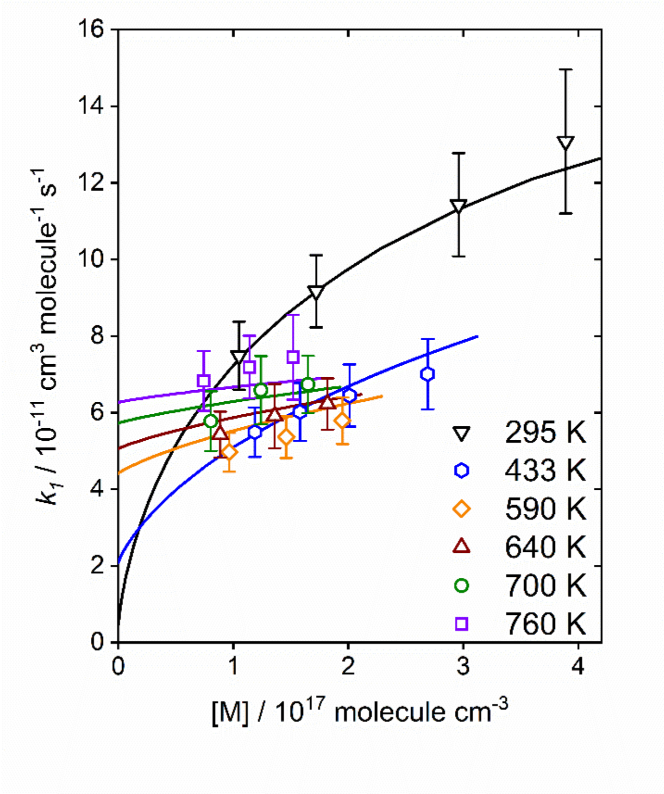

Figure 2. Pressure dependence of k_1 (AlO + H_2O) at 295 - 760 K in N_2 bath gas. The symbols are experimental values, and the lines are Master Equation fits which include contributions from R1a, R1b and R1c (see the Discussion).

AlO + H_2

The pseudo first-order decay of AlO in the presence of H_2 for the bimolecular reaction R2 can be described by:

$$k' = k_{diff} + k_2[\mathrm{H_2}] \qquad \text{(E2)}$$

Kinetic traces were satisfactorily fitted either using a single exponential decay after a time delay (as described for R1 above), or using a bi-exponential to fit both the growth and loss of the AlO signal, with both determinations of k'agreeing within error. k_2 is much slower than k_1 over the entire temperature range, so it was necessary to work with [H_2] up to 3 orders of magnitude larger than the [H_2O] needed to study R1. At such high H_2 concentrations, it is possible that secondary chemistry between H_2 and the precursor might result in reactive species that remove AlO, and thus affect the determination of k_2. To investigate this possibility, measurements of k_2 were carried out over a range of residence times in the reactor for each temperature. Changing the residence time was achieved by varying the ratios of total pressure versus the total flow rate. An example plot of the measured value of k_2 at 694 K versus the residence time is shown in Figure 3, which illustrates that k_2 increased by roughly a factor of 2 at the longest residence time (i.e. highest pressure:flow ratio). This suggests that secondary chemistry between H_2 and the Al(acac)$_3$ precursor does produce a reactive species that removes AlO, resulting in an overestimate of k_2 at the longest residence times. Since the relationship between the measured rate coefficient and the residence time is complex, extrapolating the measured k_2 to zero residence time is not straightforward. However, visual inspection of the measured rates *vs* residence time at each temperature show that at the lowest residence times the measured k_2 becomes effectively independent of residence time, suggesting little or no contribution from secondary chemistry. Thus, the final values reported for k_2 at each temperature are only those obtained at the shortest residence times, where the measured value was essentially independent of residence time (Figure 3). The rates obtained using this visual inspection method are in good agreement with rates obtained by extrapolating to zero residence time using an exponential function, but are around 40% higher than rates obtained extrapolating using a linear fit. The values of k_2 over the range of temperature and pressure conditions studied are listed in Table S1.

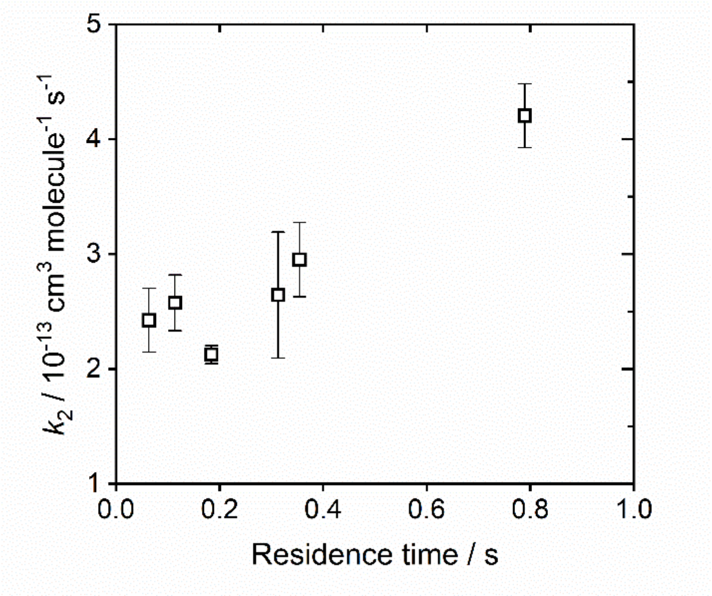

Figure 3. Bimolecular rate coefficients (k_2) for R2 at 694 K measured at different reactor residence times in s.

The other potential problem with having to use high concentrations of H_2 was the possible presence of contaminants in the H_2, specifically H_2O and O_2 which recombine relatively rapidly with AlO (see above and Mangan *et al.* [30], respectively). To investigate this possibility and any potential termolecular channel for H_2, the pressure dependence of the AlO + H_2 reaction was investigated. In Figure 4, k_2 is plotted against total pressure (concentration [M]) over the temperature range 467 - 780 K. A H_2O leak on its own would only account for a 10 – 20% change in k_2 with pressure at each temperature studied, a change similar to the experimental error. However, H_2O contamination would have had to come from an air leak, so that the recombination reaction of AlO with O_2 must also be included. If there had been a sufficient air leak in the gas line from the H_2 cylinder to account for the measured k_2, this would have produced an approximately 50% increase in k_2 over the pressure range studied at 467 K, and 30% increase at 700 K. In fact, Figure 4 shows that no pressure dependent behaviour was observed within the experimental uncertainty (only 10 - 20%). This indicates the absence of both a significant leak and a termolecular channel for the H_2 reaction, further confirmed by observing no difference in k_2 measured with either N_2 or He as the bath gas (the former is roughly twice as efficient as a third body [31]). At higher temperatures, the bimolecular channel of AlO + H_2O could play a role if the H_2 were contaminated with H_2O from an air leak. However, this point is discussed further - and ruled out - in the Discussion below.

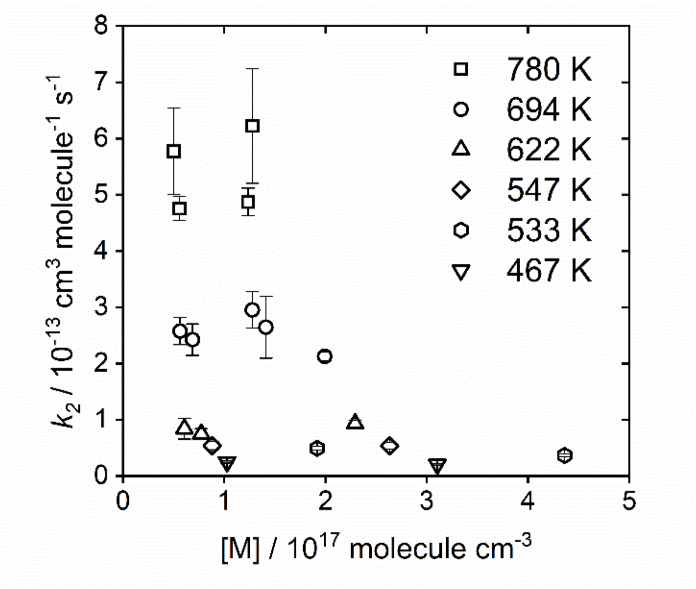

Figure 4. Plot of k_2 against the total concentration [M] in molecule cm^{-3} for the reaction of AlO + H_2 at $T = 467 - 780$ K.

k_2 was measured from 463 – 785 K, as shown in Figure 5. The low temperature limit was set by the reaction becoming too slow at lower temperatures to measure with this system, and the high temperature limit by decomposition of $Al(acac)_3$. An Arrhenius fit to the dataset (dashed line) yields $k_2(463 - 785\ K) = (5.8 \pm 2.1) \times 10^{-11} \times \exp^{(-3792 \pm 215)/T}$ cm^3 molecule^{-1} s^{-1}. The theoretical fit to the dataset (red line) and subsequent extrapolation to the higher temperatures pertinent for AGB stellar chemistry are discussed in the Discussion below.

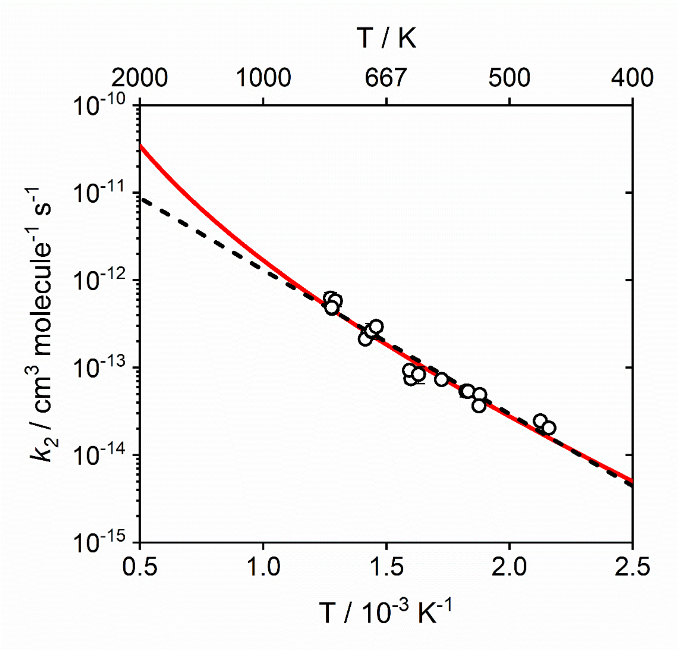

Figure 5. Temperature dependence of the measured (open black circles) bimolecular rate coefficients (k_2) for AlO + H_2. The dashed line is an Arrhenius fit to the experimental points and the red solid line is a theoretical fit using RRKM theory (see the Discussion).

Discussion

The reaction between AlO and H_2O (R1) does not appear to have been studied previously. However, in the case of AlO + H_2 (R2), Parnis *et al.* [25] measured an upper limit at 298 K of 5 × 10^{-14} cm^3 $molecule^{-1}$ s^{-1}, which is consistent with the extrapolated value of 2 × 10^{-16} cm^3 $molecule^{-1}$ s^{-1} in the present study (using the Arrhenius expression determined in the Results section). The reaction between Al and H_2O (R3) has been studied from 298 - 1174 K [26]. A number of theoretical studies of the potential energy surfaces connecting Al + H_2O with AlO + H_2, including transition state theory (TST) estimates of k_3 and k_4, have been published over the past 50 years.[32-34] These studies have mainly been driven by interest in Al combustion chemistry.

In order to extrapolate the rate coefficients measured in the present study to temperatures above 1000 K pertinent to stellar outflow chemistry, and also to determine product branching ratios, we combined electronic structure calculations of stationary points on the relevant PES with RRKM theory. Because reaction R3 (Al + H_2O) occurs on parts of the same PES as R2 (AlO + H_2), we also extrapolated the previous measurements of k_3 [26] to higher temperatures. The geometries of the Al-containing molecules were first optimized at the B3LYP/6-311+g(2d,p) level of theory within the Gaussian 16 suite of programs,[19] and then accurate energies were determined at the G4 level of theory [20]. This level of theory was chosen because it is reasonably computationally efficient and in general appears to perform well on reactions involving small Al-containing molecules (though see below). For example, the reaction enthalpy for Al + O_2 $\rightarrow$ AlO + O is calculated at the G4 level to be $\Delta H°(0\ K) = -9.9$ kJ mol^{-1}, in excellent agreement with the very high level (but computationally expensive) W1BD compound method,[35] which gives $\Delta H°(0\ K) = -10.2$ kJ mol^{-1}. These values are consistent with the experimental value of -14 ± 9 kJ mol^{-1}. [23]

The Cartesian coordinates, rotational constants, vibrational frequencies and heats of formation of the stationary points on the PESs for R1 and R2/R3 are listed in Tables S2 and S3, respectively. The PESs are shown in Figure 6, which also illustrates the geometries of these stationary points. The energies shown include zero-point energies, and this is why the energy of the saddle point labelled TS2 in Figure 6a appears slightly below that of the AlO-H_2O adduct.

RRKM calculations were then performed using the Master Equation Solver for Multi-Energy well Reactions (MESMER) program.[36] Each reaction is assumed to proceed via the formation of an excited adduct, which can either dissociate or be stabilized by collision with the N_2 third body. The internal energy of this adduct was divided into a contiguous set of grains (typical width between 100 and 150 cm^{-1}) containing a bundle of rovibrational states. Each grain was then assigned a set of microcanonical rate coefficients for dissociation, which were determined using inverse Laplace transformation to link them directly to $k_{rec,\infty}$, the high pressure limiting recombination coefficient. The density of states of each adduct was calculated with the vibrational frequencies and rotational constants listed in Table S2 or S3, without making a correction for anharmonicity, and a classical densities of states treatment for the rotational modes. The microcanonical rate coefficients for reactions over barriers were treated using RRKM theory, with Eckart tunnelling applied where an H atom transfer occurred.[36]

The probability of collisional transfer between grains was estimated using the exponential down model, where the average energy for downward transitions is designated $\langle \Delta E \rangle_{down}$, and the probabilities for upward transitions are determined by detailed balance.[31] $\langle \Delta E \rangle_{down}$ was assigned a small temperature dependence of the form T^{β}. The collision rate of N_2 with the adduct as a function of temperature, $Z(T)$, was calculated using Lennard-Jones parameters (σ and ε) to characterise the intermolecular potential. The Master Equation (ME), which describes the evolution with time of the adduct grain populations, was then expressed in matrix form and solved to yield the recombination rate constant at a specified pressure and temperature. The adjustable parameters used to perform a global fit to all the experimental data points for each reaction were $k_{\mathrm{rec},\infty}$, σ, $<\Delta E>_{\mathrm{down}}$ and β. Table 1 summarises the results.

Table 1. Parameters used in RRKM fits to the kinetics of reactions R1, R2 and R3.

Reaction	$\langle\Delta E\rangle_{\mathrm{down}}$ cm^{-1} at 298 K	β [a]	$k_{\mathrm{rec},\infty}$ cm^3 molecule^{-1} s^{-1}	$Z(T)$ [b] cm^3 molecule^{-1} s^{-1}
AlO + H_2O (R1)	290	-0.5	7.0×10^{-10} exp(-265/T)	3.43×10^{-10} $(T/298)^{0.178}$
AlO + H_2 (R2)	300	0.0	Not applicable since first step is over a significant barrier – see Fig. 6(b)	2.52×10^{-10} $(T/298)^{0.178}$
Al + H_2O (R3)	300	0	3.0×10^{-11} $(T/298)^{0.167}$	2.52×10^{-10} $(T/298)^{0.178}$

[a] $\langle\Delta E\rangle_{\mathrm{down}}(T) = \langle\Delta E\rangle_{\mathrm{down}}(T / 298)^{\beta}$

[b] Collision frequency between the adduct and N_2. For R1, σ = 3.5 Å and ε/k_B = 300 K; for R2 and R3, σ = 3.0 Å and ε/k_B = 300 K.

AlO + H_2O

The recombination reaction R1a has a small submerged barrier (TS2 in Figure 6a) where the initial AlO-H_2O adduct rearranges to form the product $Al(OH)_2$. The well is deep (-307 kJ mol^{-1} with respect to the reactants). Hence, the recombination is very fast, and is in the fall-off region over the experimental pressure range (Figure 2). The fitted value of $<\Delta E>_{\mathrm{down}}$ of 290 cm^{-1} at 298 K is within the expected range for N_2, along with the small temperature dependence of β = -0.5.[31] The fitted Lennard-Jones parameters (footnote to Table 1) give $Z(T)$ essentially at the collision frequency. The fitted value of $k_{\mathrm{rec},\infty}$ for reaction R1 is a factor of ~2.4 times smaller than the dipole-dipole capture rate between AlO and H_2O, with a small positive temperature dependence.

The rate coefficient k_{1a} can then be expressed by a Lindemann expression modified by a broadening factor Fc [37]: $\log_{10}(k_{1\mathrm{rec},0}$ / cm^6 molecule^{-2} s^{-1}) = -32.9185 + 8.80276 $\log_{10}(T)$ - 2.4723$(\log_{10}(T))^2$; $\log_{10}(k_{1\mathrm{rec},\infty}$ / cm^3 molecule^{-1} s^{-1}) = -19.4686 + 7.62037 $\log_{10}(T)$ - 1.47214$(\log_{10}(T))^2$; Fc = 0.28, with an uncertainty of ±13% within the experimental temperature range (295 – 760 K).

In terms of AlO chemistry in planetary atmospheres, the termolecular channel R1a will usually not compete with recombination of AlO with significantly more abundant species such as O_2 and CO_2 or, in the case of the terrestrial atmosphere, bimolecular reaction with O_3.[22, 30]

The bimolecular reaction between AlO and H_2O can form either AlOH (R1b), OAlOH (R1c) or OAlO (R1d). $Al(OH)_2$ dissociates to AlOH without a barrier, although the overall reaction enthalpy of R1b is 15 kJ mol^{-1} endothermic. In contrast, the direct pathway via TS1 (blue route in Figure 6a) involves a barrier of 60 kJ mol^{-1} and so is uncompetitive. Channel R1c involves either a direct reaction over a significant barrier (red route, TS3 at 87 kJ mol^{-1}), or dissociation of $Al(OH)_2$ to OAlOH + H which is endothermic by 26 kJ mol^{-1} (Figure 6a). Reaction channel 1d to form OAlO + H_2 is very endothermic (111 kJ mol^{-1}). Hence, reaction 1b to form AlOH + OH via $Al(OH)_2$ is the dominant bimolecular reaction channel (>99% over the temperature range 300 – 1600 K):

$k_{1b}(AlO + H_2O \rightarrow AlOH + OH) = (3.89\pm0.47) \times 10^{-10} \exp(-(1295\pm150)/T)$ cm^3 molecule^{-1} s^{-1}.

This reaction channel will also very likely be too slow to be important in a planetary atmosphere.

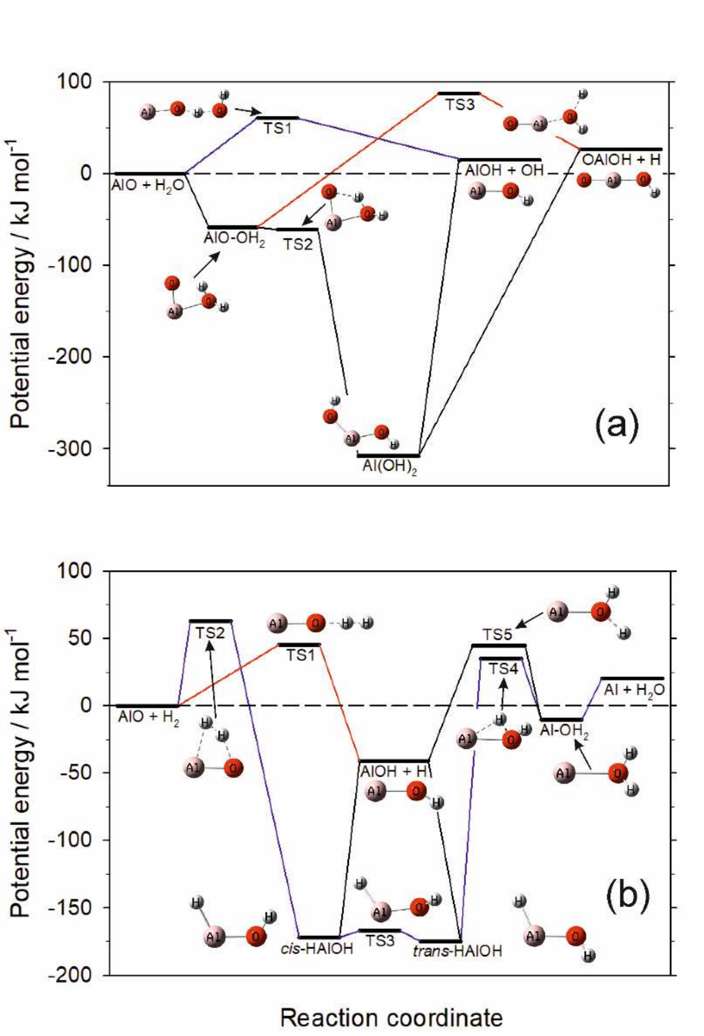

Figure 6. Potential energy surfaces for a) AlO + H_2O and b) AlO + H_2. The relative energies include zero-point energy corrections. These are calculated using the G4 quantum chemistry compound method.[38]

AlO + H_2

The PES for this reaction is illustrated in Figure 6b. It is generally in good agreement with three relatively recent theoretical studies,[33, 34], particularly with Sharipov *et al.* [33] who used G3 theory. The products AlOH + H can be formed directly through H atom abstraction via TS1, or indirectly via insertion of the AlO into the H-H bond via TS2 to form *cis*-HAlOH or *trans*-HAlOH (connected by TS3), which can then dissociate to AlOH + H. As shown in Figure 6b, TS1 is 17 kJ mol^{-1} lower than TS2, and so the direct pathway (red line in Fig. 6b) should be the dominant pathway. In fact, it was not possible to match the experimental points with a TS1 barrier height of 45 kJ mol^{-1} above the reactant energy. When this was reduced to 31 kJ mol^{-1}, a satisfactory fit was achieved to the experimental data points from the present study (Figure 5, red line). Although this difference of 14 kJ mol^{-1} is greater than the average absolute deviation of 5 kJ mol^{-1} for energies of non-hydrogen molecules at the G4 level of theory,[20] several of the significant outliers (> 10 kJ mol^{-1} absolute difference) in that study are Al-containing molecules.

A possible explanation for the measured rate of R2 being faster than predicted with the calculated TS1 barrier of 45 kJ mol^{-1} would be contamination of the H_2 with a leak of humid lab air, since the bimolecular channel AlO + H_2O (R1b) starts to become rapid above 500 K. However, this possibility can be ruled out because the activation energy measured for k_2 is 32 kJ mol^{-1}, which is much larger than the 11 kJ mol^{-1} measured for k_{1b} (see above). Moreover, to account for the apparent rate increase at 540 K would require a 7.5% air contamination in the H_2 flow (at the measured lab relative humidity of 40%). At the highest experimental temperature of 785 K, the H_2 flow would need to be more than 50% contaminated with room air to explain the difference between k_2 calculated using the G4 theory barrier height and the measured value.

The best fit to the experimental points in Figure 5 gives (400 - 2000 K):

$$k_2(\mathrm{AlO} + \mathrm{H_2} \rightarrow \mathrm{AlOH} + \mathrm{H}) = (5.37\pm0.52) \times 10^{-13}\ (T/300)^{(2.77\pm0.19)} \exp(-(2190\pm110)/T)\ \mathrm{cm^3\ molecule^{-1}\ s^{-1}},$$

with an uncertainty of ±23% within the experimental temperature range (463 – 785 K). At 800 K, more than 99% of the reaction product is AlOH + H; 96.3% of the AlOH is formed via TS1, 2.3% from dissociation of *cis*-HAlOH, and 1.4% from dissociation of *trans*-HAlOH. The other product, Al + H_2O which is produced via the blue route in Figure 6b, is negligible (0.008%)

Al + H_2O and AlOH + H

The same PES for reaction R2 can now be used to estimate rate coefficients for k_3 and k_4. As shown in Figure 7a, a satisfactory fit to the experimental measurements of McClean *et al.* [26] is achieved, yielding (250-1200 K):

$$k_3(\mathrm{Al} + \mathrm{H_2O} \rightarrow \mathrm{AlOH} + \mathrm{OH}) = (1.7\pm0.2) \times 10^{-12} \exp(-(422\pm50)/T) + (1.5\pm0.4) \times 10^{-10} \exp(-(2657\pm190)/T)\ \mathrm{cm^3\ molecule^{-1}\ s^{-1}}.$$

The MESMER calculation captures the experimental data below 600 K significantly better than the canonical variational theory fit of Sharipov *et al.* [33], as shown in Figure 7a. AlOH is predicted to be the only significant product (>99%). At 300 K, 19% of the AlOH is formed via TS5 (Figure 6b), 42% via TS4 and *trans*-HAlOH, and 39% via TS3, TS4 and *cis*-AlOH. The amount of AlO, formed via TS4, TS3 and TS2, is negligible (1.8×10^{-4} %).

The calculated rate coefficients for the two reaction channels of AlOH + H (R4) are shown as a function of temperature in Figure 7b. Arrhenius behaviour is predicted from 700 – 2000 K:

$$k_{4a}(\mathrm{AlOH} + \mathrm{H} \rightarrow \mathrm{AlO} + \mathrm{H_2}) = 8.89 \times 10^{-11} \exp(-9092/T)\ \mathrm{cm^3\ molecule^{-1}\ s^{-1}}$$

$$k_{4b}(\mathrm{AlOH} + \mathrm{H} \rightarrow \mathrm{Al} + \mathrm{H_2O}) = 4.31 \times 10^{-11} \exp(-9457/T)\ \mathrm{cm^3\ molecule^{-1}\ s^{-1}}$$

The ratio of AlO to Al product ranges from 2.5 to 3.5 over this temperature range. For channel R4a at 1300 K, AlO + H_2 is produced via TS1 (94%) and TS2 (6%); for channel R4b, Al + H_2O is produced via TS4 (52%) and TS5 (48%) (see Figure 6b). For reasons that are unclear, although the activation energy of 8762 K calculated by Sharipov *et al.* [33] for k_{4a} is in good agreement with the present result, the pre-exponential factor (between 700 and 2000 K) is a factor of 260 times smaller. That study did not consider the other significant channel which produces Al + H_2O (R4b).

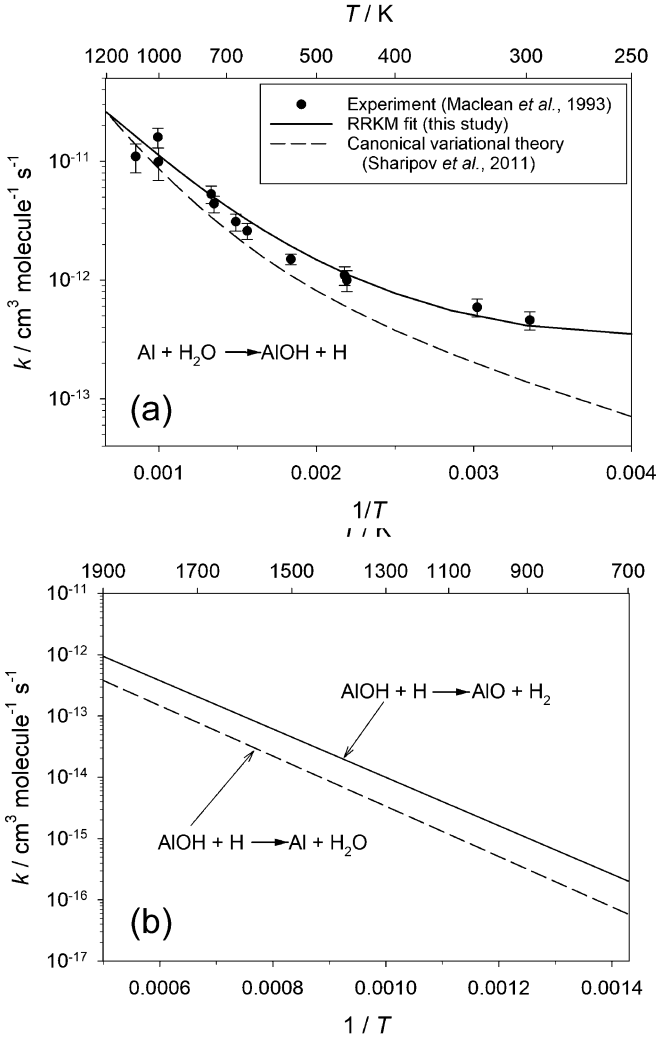

Figure 7. (a) RRKM fit (black line) to the experimental rate coefficients (points with error bars) from Maclean *et al.* [26] for the reaction between Al and H_2O. A canonical variational theory fit from Sharipov *et al.* [33] is also shown. (b) Theoretical rate coefficients for the reaction of AlOH with H, producing either Al + H_2O or AlO + H_2.

Implications on the chemistry of AlO and AlOH around an AGB star

We now incorporate these results on R1 – R4 in a model of the outflow from an AGB star, where the radial position *r* from the star is expressed as a factor of R_* (where $1R_*$ is the radius at the stellar surface). As an example, we consider a Semi-Regular Variable (SRV) star.[39] Here we model the stellar outflow with a beta-velocity law, which takes into account the net acceleration of the wind without explicitly considering pulsations:

$$v_\beta(r) = v_0 + (v_\infty - v_0)(1 - R_*/r)^\beta \qquad \text{(E3)}$$

where v_∞ is the terminal velocity, which is 5.7 km s^{-1} for the SRV model,[14] $v_0 = v(R_*) = 1.5$ km s^{-1} is the initial velocity at the stellar surface R_* (= 2.5×10^{13} cm), and the parameter $\beta = 1$. The temperature profile is given as a power-law with an exponent α = 0.6 and the density is expressed using the pressure scale height $H = RT\, R_*^2/\,(\mu M_*\, G)$, the Ideal Gas Law, and a parameter $\gamma = 0.89$ (for details, see e.g. Gobrecht *et al.* [16] and references therein):

$$T(r) = T_*(r/R_*)^{-\alpha} \qquad \text{(E4)}$$

and $$n(r) = n_* \exp((R_*(1 - \gamma^2)/(H(1 - \alpha))\,(1 - r/R_*)^{\alpha-1}) \qquad \text{(E5)}$$

The surface pressure $n_* = 10^{14}$ cm^{-3} and the effective temperature T_* is 2400 K.

The chemistry is modelled using a kinetic network which is solved with the FORTRAN routine LSODE.[40] The network includes 40 neutral molecular species and 105 reactions pertaining to the circumstellar environments of O-rich stars. Here, we assume a C/O ratio of 0.75 corresponding to the FRUITY stellar evolution model of a solar metallicity (Z=0.014) star with an initial mass of 1.5 M$_*$, having experienced 3 (out of a total of 5) dredge-up mixing episodes.[41] The species in the network include the prevalent species H_2, H, CO, CO_2, H_2O, OH and SiO.[42]. The rate coefficients are adopted from the NIST kinetics database.[43] The densities of H_2, H and H_2O (relevant for R1 to R4), as well as the temperature *T*, are illustrated in Figure 8a as a function of radial position expressed as a factor of R_*.

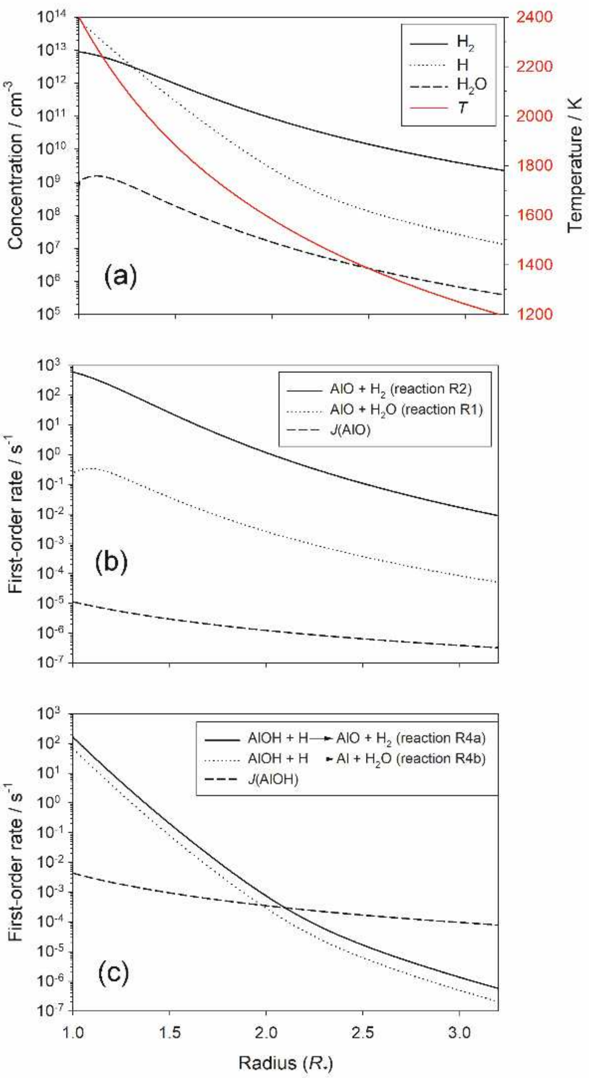

Figure 8. (a) Predicted densities of H_2, H, H_2O and T as a function of radial position for the β-velocity trajectory model of a SRV star. (b) and (c) First-order removal rates of AlO and AlOH, respectively, as a function of radius.

The photolysis rates of AlOH and AlO were computed by using the time-dependent density function theory (TD-DFT) method [44] to calculate the vertical excitation energies and transition dipole moments for transitions from the ground state of each molecule up to the first 30 electronically excited states. The resulting absorption cross sections are illustrated in Figure 9. Each cross section was then convolved up to its dissociation threshold with a model stellar irradiance flux from the MARCS data-base for an evolved star with $T_* = 2500$ K (the lowest stellar T_* in the MARCS data-base).[45] The irradiance spectrum is plotted in Figure 9. The photolysis threshold was set to correspond to the bond dissociation energy at the G4 level of theory, which is an upper wavelength limit. This is because a photon with more than the bond energy may be required depending on the position of the upper dissociating electronic states, which have been explored in detail by Trabelsi and Francisco [46]. These thermodynamic thresholds are illustrated in Figure 9. When computing the photolysis rate as a function of increasing temperature, the threshold was red-shifted to take account of the increasing internal energy of the molecule. We also assume here that AlOH photolyses to AlO + H rather than Al + OH (which is 76 kJ mol^{-1} higher in energy).

The resulting first-order photolysis rates are then: $J(\text{AlOH}) = 1.5 \times 10^{-4} \exp(1.40 \times 10^{-3}\, T)$, and $J(\text{AlO}) = 9.7 \times 10^{-7} \exp(1.02 \times 10^{-3}\, T)$ at $1R_*$. At a temperature of 2000 K, photolysis of AlOH is predicted to be 500 times faster than photolysis of AlO. This arises because although AlO has relatively large absorption features in the near-UV/visible, these are beyond its photolysis threshold, and stellar irradiance falls rapidly in the near UV (Figure 9). We assume that in the inner wind the dust-to-gas ratio is too small [5, 16] for optical extinction by dust to significantly attenuate these rates.

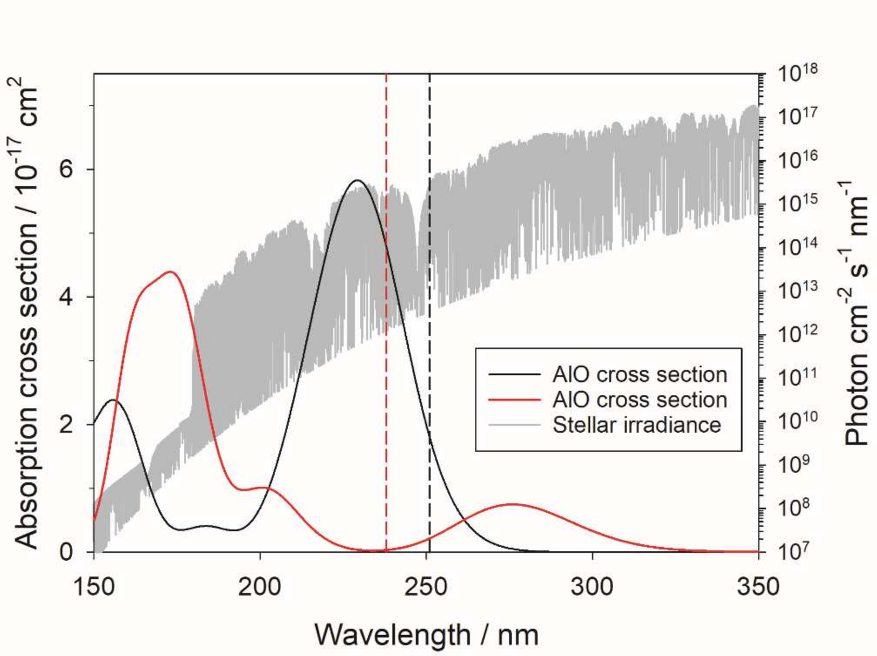

Figure 9. Absorption cross sections of AlOH and AlO computed using time-dependent density function theory.[19] The vertical dashed lines indicate the photolysis thresholds at 252 and 237 nm, respectively, computed from the relevant bond dissociation energies. Also shown (right-hand ordinate axis) is the spectral irradiance at the surface of an evolved star with an effective temperature of 2500 K, derived from the MARCS data-base.[45]

Figure 8(b) and (c) show the first-order removal rates of AlO and AlOH, respectively, as a function of r. The reaction rates generally decrease with stellar distance because of the decreasing densities of the excess reactants (H_2, H and H_2O) and temperature (Figure 8a). J(AlO) and J(AlOH) decrease as r^{2}. With the caveat that J(AlOH) is an upper limit, this photolysis rate could exceed the rate of reaction of AlOH with H (R4) at distances larger than ~2.2R_* (Figure 8c).

Note that the first-order rates in Figure 8 are faster than 10^{-7} s^{-1} at distances out to 3R_*. The expansion rate of the outflow is given by $v_\beta(r)/r$, which varies between 7×10^{-9} and 5×10^{-9} s^{-1} over this distance. Hence, the rate of chemical conversion between AlO, AlOH and Al is much faster than the expansion rate, and the kinetic steady state approximation can be applied. For this simple model which only involves these three Al-containing species, the total Al density $[Al]_{total}$ = [Al] + [AlO] + [AlOH], which we set equal to its photospheric abundance 2.82×10^{-6} relative to H (= $2[H_2]$ + [H]).[47] At steady-state,

$$[\mathrm{AlOH}] = [\mathrm{Al}_{\mathrm{total}}] \Big/ \left(1 + \frac{k_{4b}[\mathrm{H}]}{k_3[\mathrm{H_2O}]} + \left(1 + \frac{J_{\mathrm{AlO}}}{k_3[\mathrm{H_2O}]}\right)\left(\frac{k_{4a}[\mathrm{H}]+J_{\mathrm{AlOH}}}{k_{1b}[\mathrm{H_2O}]+k_{2a}[\mathrm{H_2}]+J_{\mathrm{AlO}}}\right)\right) \quad \text{(E6)}$$

$$[\mathrm{AlO}] = \left(\frac{k_{4a}[\mathrm{H}]+J_{\mathrm{AlOH}}}{k_{1b}[\mathrm{H_2O}]+k_{2a}[\mathrm{H_2}]+J_{\mathrm{AlO}}}\right)[\mathrm{AlOH}] \quad \text{(E7)}$$

and $$[\mathrm{Al}] = [\mathrm{Al}_{\mathrm{total}}] - [\mathrm{AlOH}] - [\mathrm{AlO}] \quad \text{(E8)}$$

Figure 10 illustrates the abundances of Al, AlO and AlOH with respect to the total gas density (i.e. [H] + $[H_2]$), as a function of r. The uncertainty envelopes for each species were determined using a Monte Carlo procedure to calculate the standard deviations of 1000 model runs in which k_{1b}, k_{2a}, and k_3 were randomly sampled within their 1σ uncertainties (using the uncertainties in the rate coefficient expressions in the earlier parts of the Discussion). k_{4a} and k_{4b} were estimated by detailed balance with k_{2a} and k_3, respectively, including random sampling within a ±6 kJ mol^{-1} uncertainty in the reaction enthalpies of R2a and R3 (the expected uncertainty of G4 theory[20]). AlOH becomes the most abundant Al species at $r > 1.8R_*$, tracking the increasing ratio of H_2 to H which exceeds unity at around 1.3R_* (Figure 9a), allowing R2 to dominate over R4.

The red dashed line in Figure 10 shows the AlO profile when photolysis is turned off: this relatively minor species decreases by about two orders of magnitude at a distance of 3R_*. The corresponding change in AlOH is relatively small (increase of only 0.8%) because it is already overwhelmingly the dominant Al species. Recent observations [14, 48] have detected AlO in the inner winds of SRV type stars with abundances of the order of 10^{-8}. The modelled AlO approaches 3×10^{-8} at 3R_* (Figure 10), and so is clearly in accord with these observations. Even without photolysis, AlO reaches 3×10^{-9} at 1.6R_*, which is only a factor of 3 below the observations (which in turn are quite uncertain because of assumptions that have to be made about thermodynamic quantities in the CSE).

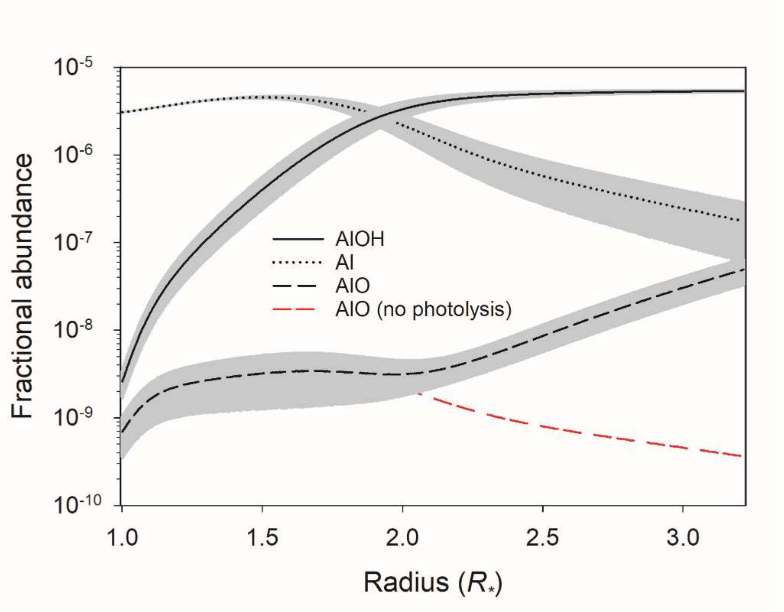

Figure 10. Fractional abundances of AlOH, AlO and Al with respect to the total gas density (i.e. H + H_2), as a function of the radial position R_* (black curves, filled grey areas are uncertainty envelopes), predicted by the SRV model with a β-velocity trajectory and steady-state kinetics. The red dashed line indicates the AlO abundance when photolysis of AlOH and AlO is turned off.

In contrast, observations of AlOH around AGB stars show that the abundance of this molecule is $\leq 10^{-7}$, [14] compared with a value of 5×10^{-6} in our model. There are two likely reasons for the model overprediction by a factor of more than 50: first is that pulsation-induced shocks,[16] which involve rapid heating that would recycle the AlOH to Al, are not included in our simple outflow model; and second, much of the Al eventually becomes locked up in alumina nanoparticles (see the Introduction), rather than remaining in the gas phase.

Finally, Figure 10 shows that the [AlO]/[AlOH] ratio beyond $1.8R_*$ depends strongly on the inclusion of AlOH photolysis. An experimental measurement of the AlOH photolysis cross section should therefore be a priority in future laboratory work.

Conclusions

The reactions of AlO with H_2O and H_2 were measured using the PLP-LIF technique in a temperature-controlled slow flow reactor. The full set of measured rate coefficients for the reactions AlO + H_2O (R1) and AlO + H_2 (R2) are listed in Table S1. These reactions were shown to occur via multiple pathways over complex potential energy surfaces. The surface for R2 also describe the reactions between Al + H_2O (R3) and AlOH + H (R4). Satisfactory fits of a Master Equation solver for reactions with multiple energy wells to the experimental data provide the rate coefficient expressions for R1 – R4 summarized in Table 2. These are appropriate for modelling Al chemistry in stellar outflows and planetary upper atmospheres.

In the inner region of the outflow from an evolved star, where not enough dust has been produced to cause significant optical extinction in the near-UV, the photolysis of AlOH and AlO needs to be considered. Upper limits to the photolysis rates of these molecules were estimated by calculating their absorption cross sections and setting the photodissociation threshold equal to the relevant bond energy, as well as assuming that AlOH only photolyses to

AlO. The stellar outflow chemistry of Al was then investigated using a β-trajectory model of a Semi-Regular Variable AGB star, where the kinetic steady-state approximation is valid. This relatively simple model predicts that AlOH is the major gas-phase Al species beyond two stellar radii, and shows that the relative AlO abundance is very sensitive to the AlOH photolysis rate.

Table 2. Summary of rate coefficients determined in this study.

	Reaction	Rate coefficient[a]
R1a	$AlO + H_2O (+ N_2) \rightarrow Al(OH)_2$	$\log_{10}(k_{1rec,0}$ / cm^6 molecule^{-2} s^{-1}) = -32.9185 + 8.80276 $\log_{10}(T)$ - 2.4723$(\log_{10}(T))^2$; $\log_{10}(k_{1rec,\infty}$ / cm^3 molecule^{-1} s^{-1}) = -19.4686 + 7.62037 $\log_{10}(T)$ - 1.47214$(\log_{10}(T))^2$; $Fc = 0.28$ (uncertainty ±13% from 295 – 760 K)
R1b	$AlO + H_2O \rightarrow AlOH + OH$	$(3.89\pm0.47) \times 10^{-10} \exp(-(1295\pm150)/T)$
R2a	$AlO + H_2 \rightarrow AlOH + H$	$(5.37\pm0.52) \times 10^{-13} (T/300)^{(2.77\pm0.19)} \exp(-(2190\pm110)/T)$
R3	$Al + H_2O \rightarrow AlOH + H$	$(1.7\pm0.2) \times 10^{-12} \exp(-(422\pm50)/T) + (1.5\pm0.4) \times 10^{-10} \exp(-(2657\pm190)/T)$
R4a	$AlOH + H \rightarrow AlO + H_2$	$8.89 \times 10^{-11} \exp(-9092/T)$ [b]
R4b	$AlOH + H \rightarrow Al + H_2O$	$4.31 \times 10^{-11} \exp(-9457/T)$ [b]

[a] Units for bimolecular reactions: cm^3 molecule^{-1} s^{-1}. [b] Theoretical estimates, not fitted to experimental data.

Supporting Information: Table S1 provides a list of second-order rate coefficients measured for reactions R1 and R2, as a function of temperature and pressure (and bath gas for R2). Table S2 lists the molecular properties and heats of formation (at 0 K) of the stationary points on the $AlO + H_2O$ potential energy surface. Table S3 lists the molecular properties and heats of formation (at 0 K) of the stationary points on the $AlO + H_2$ potential energy surface.

Acknowledgements

This work was supported by the European Research Council (Consolidator grant 646758AEROSOL) and the UK Natural Environment Research Council (Grant Number NE/P001815/1). The kinetic data and the parameters used in the theoretical calculations are provided in the Supporting Information. The data plotted in Figures 8 -10 is available at doi:10.5281/zenodo.5017759.

References

(1). Gail, H. P.; Zhukovska, S. V.; Hoppe, P.; Trieloff, M. Stardust from asymptotic giant branch stars. *Astrophys. J.* **2009,** *698*, 1136-1154.

(2). Gehrz, R. D. Sources of Stardust in the Galaxy. In *Interstellar Dust. International Astronomical Union*, Allamandola, L. J.; Tielens, A. G. G. M., Eds. Springer, Dordrecht: 1989; Vol. 135, pp 445-453.

(3). Bromley, S. T.; Martin, J. C. G.; Plane, J. M. C. Under what conditions does $(SiO)_N$ nucleation occur? A bottom-up kinetic modelling evaluation. *Phys. Chem. Chem. Phys.* **2016,** *18*, 26913-26922; Gail, H. P.; Wetzel, S.; Pucci, A.; Tamanai, A. Seed particle formation for silicate dust condensation by SiO nucleation. *Astron. Astrophys.* **2013,** *555*, art. no.: A119; Gail, H. P.; Sedlmayr, E. Mineral formation in stellar winds. I. Condensation sequence of silicate and iron grains in stationary oxygen rich outflows. *Astron. Astrophys.* **1999,** *347*, art. no.: 594; Plane, J. M. C. On the nucleation of dust in oxygen-rich stellar outflows. *Phil. Trans. Roy. Soc. A* **2013,** *371*, art. no.: 20120335.

(4). Sargent, B. A. Alumina Polymorphism in the Circumstellar Dust Shells of Asymptotic Giant Branch Stars. *Astrophys. J.* **2018,** *866*, art. no.: L1.

(5). Karovicova, I.; Wittkowski, M.; Ohnaka, K.; Boboltz, D. A.; Fossat, E.; Scholz, M. New insights into the dust formation of oxygen-rich AGB stars. *Astron. Astrophys.* **2013,** *560*, art. no.: A75.

(6). Onaka, T.; de Jong, T.; Willems, F. J. A study of M Mira variables based on IRAS LRS observations. I. Dust formation in the circumstellar shell. *Astron. Astrophys.* **1989,** *218*, 169-179.

(7). Takigawa, A.; Kamizuka, T.; Tachibana, S.; Yamamura, I. Dust formation and wind acceleration around the aluminum oxide–rich AGB star W Hydrae. *Science Adv.* **2017,** *3*, art. no.: eaao2149.

(8). Begemann, B.; Dorschner, J.; Henning, T.; Mutschke, H.; Gurtler, J.; Kompe, C.; Nass, R. Aluminum oxide and the opacity of oxygen-rich circumstellar dust in the 12-17 micron range. *Astrophys. J.* **1997,** *476*, 199-208.

(9). Posch, T.; Kerschbaum, F.; Mutschke, H.; Fabian, D.; Dorschner, J.; Hron, J. On the origin of the 13 mu m feature - A study of ISO-SWS spectra of oxygen-rich AGB stars. *Astron. Astrophys.* **1999,** *352*, 609-618.

(10). Sloan, G. C.; Kraemer, K. E.; Goebel, J. H.; Price, S. D. Guilt by association: The 13 micron dust emission feature and its correlation to other gas and dust features. *Astrophys. J.* **2003,** *594*, 483-495.

(11). Jones, O. C.; Kemper, F.; Srinivasan, S.; McDonald, I.; Sloan, G. C.; Zijlstra, A. A. Modelling the alumina abundance of oxygen-rich evolved stars in the Large Magellanic Cloud. *Mon. Not. Roy. Astron. Soc.* **2014,** *440*, 631-651.

(12). Tenenbaum, E. D.; Ziurys, L. M. Exotic Metal Molecules in Oxygen-rich Envelopes: Detection of AlOH ($X^1\Sigma^+$) in VY Canis Majoris. *Astrophy. J. Lett.* **2010,** *712*, art. no.: L93.

(13). Kamiński, T.; Wong, K. T.; Schmidt, M. R.; Müller, H. S. P.; Gottlieb, C. A.; Cherchneff, I.; Menten, K. M.; Keller, D.; Brünken, S.; Winters, J. M., et al. An observational study of dust nucleation in Mira (o Ceti) I. Variable features of AlO and other Al-bearing species. *Astron. Astrophys.* **2016,** *592*, art. no.: A42; De Beck, E.; Decin, L.; Ramstedt, S.; Olofsson, H.; Menten, K. M.; Patel, N. A.; Vlemmings, W. H. T. Search for aluminium monoxide in the winds of oxygen-rich AGB stars. *Astron. Astrophys.* **2017,** *598*, art. no.: A53.

(14). Decin, L.; Richards, A. M. S.; Waters, L. B. F. M.; Danilovich, T.; Gobrecht, D.; Khouri, T.; Homan, W.; Bakker, J. M.; Van de Sande, M.; Nuth, J. A., et al. Study of the aluminium content in AGB winds using ALMA. *Astron. Astrophys.* **2017,** *608*, art. no.: A55.

(15). Tachibana, S.; Kamizuka, T.; Hirota, T.; Sakai, N.; Oya, Y.; Takigawa, A.; Yamamoto, S. Spatial Distribution of AlO in a High-mass Protostar Candidate Orion Source I. *Astrophys. J.* **2019,** *875*, art. no.: L29.

(16). Gobrecht, D.; Cherchneff, I.; Sarangi, A.; Plane, J. M. C.; Bromley, S. T. Dust formation in the oxygen-rich AGB star IK Tauri. *Astron. Astrophys.* **2016,** *585*, art. no.: A6.

(17). Álvarez-Barcia, S.; Flores, J. R. Can alumina particles be formed from Al hydroxide in the circumstellar media? A first-principles chemical study. *Phys. Chem. Chem. Phys.* **2016,** *18*, 6103-6112.

(18). Decin, L.; Justtanont, K.; De Beck, E.; Lombaert, R.; de Koter, A.; Waters, L. B. F. M.; Marston, A. P.; Teyssier, D.; Schöier, F. L.; Bujarrabal, V., et al. Water content and wind acceleration in the envelope around the oxygen-rich AGB star IK Tauri as seen by Herschel/HIFI. *Astron. Astrophys.* **2010,** *521*, art. no.: L4.

(19). Frisch, M. J.; Trucks, G. W.; Schlegel, H. B.; Scuseria, G. E.; Robb, M. A.; Cheeseman, J. R.; Scalmani, G.; Barone, V.; Petersson, G. A.; Nakatsuji, H., et al. *Gaussian 16, Revision B.01*, Gaussian, Inc.: Wallingford, CT, USA, 2016.

(20). Curtiss, L. A.; Redfern, P. C.; Raghavachari, K. Gaussian-4 theory. *J. Chem. Phys.* **2007,** *126*, art. no.: 084108.

(21). Carrillo-Sánchez, J. D.; Gómez-Martín, J. C.; Bones, D. L.; Nesvorný, D.; Pokorný, P.; Benna, M.; Flynn, G. J.; Plane, J. M. C. Cosmic dust fluxes in the atmospheres of Earth, Mars, and Venus. *Icarus* **2020,** *335*, art. no.: 113395.

(22). Plane, J. M. C.; Daly, S. M.; Feng, W. H.; Gerding, M.; Martin, J. C. G. Meteor-Ablated Aluminum in the Mesosphere-Lower Thermosphere. *J. Geophys. Res.-Space Phys.* **2021,** *126*, art. no.: e2020JA028792.

(23). Gómez Martín, J. C.; Daly, S. M.; Brooke, J. S. A.; Plane, J. M. C. Absorption cross sections and kinetics of formation of AlO at 298K. *Chem. Phys. Lett.* **2017,** *675*, 56-62.

(24). Plane, J. M. C.; Flynn, G. J.; Määttänen, A.; Moores, J. E.; Poppe, A. R.; Carrillo-Sanchez, J. D.; Listowski, C. Impacts of cosmic dust on planetary atmospheres and surfaces. *Space Sci. Rev.* **2017,** *214*, art. no.: 23.

(25). Parnis, J. M.; Mitchell, S. A.; Kanigan, T. S.; Hackett, P. A. Gas-phase reactions of AlO with small molecules. *J. Phys. Chem.* **1989,** *93*, 8045-8052.

(26). McClean, R. E.; Nelson, H. H.; Campbell, M. L. Kintetics of the reaction Al(^{2}P) over an extended temperature range. *J. Phys. Chem.* **1993,** *97*, 9673-9676.

(27). Mangan, T. P.; McAdam, N.; Daly, S. M.; Plane, J. M. C. Kinetic Study of Ni and NiO Reactions Pertinent to the Earth's Upper Atmosphere. *J. Phys. Chem. A* **2019,** *123*, 601-610.

(28). Teghil, R.; Ferro, D.; Bencivenni, L.; Pelino, M. A thermodynamic study of the sublimation processes of aluminium and copper acetylacetonates. *Thermochimica Acta* **1981,** *44*, 213-222.

(29). Saksena, M. D.; Deo, M. N.; Sunanda, K.; Behere, S. H.; Londhe, C. T. Fourier transform spectral study of $B^2\Sigma^+–X^2\Sigma^+$ system of AlO. *J. Molec. Spectr.* **2008,** *247*, 47-56.

(30). Mangan, T. P.; Harman-Thomas, J. M.; Lade, R. E.; Douglas, K. M.; Plane, J. M. C. Kinetic Study of the Reactions of AlO and OAlO Relevant to Planetary Mesospheres. *ACS Earth Space Chem.* **2020,** *4*, 2007-2017.

(31). Gilbert, R. G.; Smith, S. C. *Theory of Unimolecular and Recombination Reactions*. Blackwell: Oxford, 1990.

(32). Mayer, S. W.; Schieler, L.; Johnston, H. S. Computation of high-temperature rate constants for bimolecular reactions of combustion products. *Symp. Int. Combust. Proc.* **1967,** *11*, 837 - 844.

(33). Sharipov, A.; Titova, N.; Starik, A. Kinetics of Al+H_2O Reaction: Theoretical Study. *J. Phys. Chem. A* **2011,** *115*, 4476-4481.

(34). Álvarez-Barcia, S.; Flores, J. R. A theoretical study of the dynamics of the Al + H_2O reaction in the gas-phase. *Chem. Phys.* **2011,** *382*, 92-97; Sun, Y.; Tian, Y.; Li, S. Theoretical Study on Reaction Mechanism of Aluminum-Water System. *Chin. J. Chem. Phys.* **2008,** *21*, 245 - 249.

(35). Barnes, E. C.; Petersson, G. A.; Montgomery, J. A.; Frisch, M. J.; Martin, J. M. L. Unrestricted Coupled Cluster and Brueckner Doubles Variations of W1 Theory. *J. Chem. Theory Comput.* **2009,** *5*, 2687-2693.

(36). Glowacki, D. R.; Liang, C.-H.; Morley, C.; Pilling, M. J.; Robertson, S. H. MESMER: An Open-Source Master Equation Solver for Multi-Energy Well Reactions. *J. Phys. Chem. A* **2012,** *116*, 9545−9560.

(37). Rollason, R. J.; Plane, J. M. C. A Kinetic Study of the Reactions of MgO with H_2O, CO_2 and O_2: Implications for Magnesium Chemistry in the Mesosphere. *Phys. Chem. Chem. Phys.* **2001,** *3*, 4733-4740.

(38). Curtiss, L. A.; Redfern, P. C.; Raghavachari, K. Gaussian-4 theory. *J. Chem. Phys.* **2007,** *126*, art. no.: 084108.

(39). Feast, M. W. The pulsation, temperatures and metallicities of Mira and semiregular variables in different stellar systems. *Mon. Not. Roy. Astron. Soc.* **1996,** *278*, 11-21; Olofsson, H.; González Delgado, D.; Kerschbaum, F.; Schöier, F. L. Mass loss rates of a sample of irregular and semiregular M-type AGB-variables. *Astron. Astrophys.* **2002,** *391*, 1053-1067.

(40). Hindmarsh, A. C. LSODE and LSODI, two new initial value ordinary differential equation solvers. *ACM Signum Newsletter* **1980,** *15*, 10-11.

(41). Cristallo, S.; Straniero, O.; Piersanti, L.; Gobrecht, D. Evolution, nucleosynthesis, and yields of AGB stars at different metallicities. III. Intermediate-mass models, revised low-mass models, and the pH-FRUITY interface. *Astrophys. J. Suppl. Ser.* **2015,** *219*, art. no.: 40.

(42). Höfner, S.; Olofsson, H. Mass loss of stars on the asymptotic giant branch: Mechanisms, models and measurements. *Astron. Astrophys. Rev.* **2018,** *26*, art. no.: 1.

(43). Manion, J. A.; Huie, R. E.; Levin, R. D.; D. R. Burgess Jr.; Orkin, V. L.; Tsang, W.; McGivern, W. S.; Hudgens, J. W.; Knyazev, V. D.; Atkinson, D. B., et al., NIST Chemical Kinetics Database, NIST Standard Reference Database 17, Version 7.0 (Web Version), Release 1.6.8, Data version 2015.09 National Institute of Standards and Technology: Gaithersburg, Maryland, 2021.

(44). Bauernschmitt, R.; Ahlrichs, R. Treatment of electronic excitations within the adiabatic approximation of time dependent density functional theory. *Chem. Phys. Lett.* **1996,** *256*, 454-464.

(45). Gustafsson, B.; Edvardsson, B.; Eriksson, K.; Jørgensen, U. G.; Nordlund, Å.; Plez, B. A grid of MARCS model atmospheres for late-type stars. I. Methods and general properties. *Astron. Astrophys.* **2008,** *486*, 951-970.

(46). Trabelsi, T.; Francisco, J. S. Is AlOH the Astrochemical Reservoir Molecule of AlO?: Insights from Excited Electronic States. *Astrophys. J.* **2018,** *863*, art. no.: 139.

(47). Asplund, M.; Grevesse, N.; Sauval, A. J.; Scott, P. The Chemical Composition of the Sun *Ann. Rev. Astron. Astrophys.* **2009,** *47*, 481-522.

(48). Danilovich, T.; Gottlieb, C. A.; Decin, L.; Richards, A. M. S.; Lee, K. L. K.; Kamiński, T.; Patel, N. A.; Young, K. H.; Menten, K. M. Rotational Spectra of Vibrationally Excited AlO and TiO in Oxygen-rich Stars. *Astrophys. J.* **2020,** *904*, art. no.: 110.

For Table of Contents Only